SCIENTIFIC REPORTS

OPEN

SUBJECT AREAS:
ELECTROCHEMISTRY
BATTERIES

Received
8 April 2014

Accepted
28 July 2014

Published
14 August 2014

Correspondence and requests for materials should be addressed to S.H.O. (sho74@kist.re.kr)

Electrochemically-induced reversible transition from the tunneled to layered polymorphs of manganese dioxide

Boeun Lee[1], Chong Seung Yoon[2], Hae Ri Lee[1], Kyung Yoon Chung[1], Byung Won Cho[1] & Si Hyoung Oh[1]

[1]Center for Energy Convergence Research, Korea Institute of Science and Technology, Hwarang-ro 14-gil 5, Seongbuk-gu, Seoul, 136-791, Korea, [2]Department of Materials Science and Engineering, Hanyang University, 222 Wangsimni-ro, Seongdong-gu, Seoul, 133-791, Korea.

Zn-ion batteries are emerging energy storage systems eligible for large-scale applications, such as electric vehicles. These batteries consist of totally environmentally-benign electrode materials and potentially manufactured very economically. Although Zn/α-MnO_2 systems produce high energy densities of 225 Wh kg^{-1}, larger than those of conventional Mg-ion batteries, they show significant capacity fading during long-term cycling and suffer from poor performance at high current rates. To solve these problems, the concrete reaction mechanism between α-MnO_2 and zinc ions that occur on the cathode must be elucidated. Here, we report the intercalation mechanism of zinc ions into α-MnO_2 during discharge, which involves a reversible phase transition of MnO_2 from tunneled to layered polymorphs by electrochemical reactions. This transition is initiated by the dissolution of manganese from α-MnO_2 during discharge process to form layered Zn-birnessite. The original tunneled structure is recovered by the incorporation of manganese ions back into the layers of Zn-birnessite during charge process.

For thousands of years, manganese oxides with various layered and tunneled structures have been extensively used by mankind[1,2]. These materials show superb catalytic activities for many chemical processes, such as oxygen reduction reaction in metal-air cells[3], and function as good oxidants in many organic syntheses[4]. They also act as geochemical scavengers for metals commonly found in soils[5]. Since they are one of the major natural constituents of ocean Mn nodules, bottoms of fresh-water lakes, and river-beds, they are abundant and environmentally benign. Although some types of MnO_2 materials (γ-MnO_2) are already widely used commercially in alkaline batteries[6], they are gaining reviving attention as promising electrode materials for 'Zn-ion batteries', an emerging energy storage system developed for medium- to large-scale applications, such as electric vehicles and load-leveling of intermittent power sources[7–9]. Recently, as the demand for safe, low cost energy storage systems with high power densities has intensified, a variety of new energy storage systems based on multivalent cation charge carriers, such as Mg^{2+}, Zn^{2+}, and Al^{3+} ions, have begun to be investigated[7–13]. Among them, Zn-ion batteries have gained world-wide attention as one of the most viable candidates for replacing conventional Li-ion batteries in the near future. Zn-ion batteries consist of environmentally benign electrode materials, that is, a MnO_2 cathode and zinc metal anode, and employ a simple aqueous electrolyte system. Hence, they can potentially be manufactured very economically. Zn-ion batteries can employ many forms of polymorphic MnO_2, including α-MnO_2, β-MnO_2, γ-MnO_2, λ-MnO_2, and todorokite as cathode materials that can incorporate zinc ions into their tunneled structures. Specifically, α-MnO_2 can produce large discharge capacities: as large as 210 mAh g^{-1}, with a practical discharge potential of 1.3 V at a moderate current rate, leading to an energy density of 225 Wh kg^{-1} based on the weight of the cathode and anode materials[7–9]. This is substantially larger than values reported for competing multivalent-ion charge carrier systems, such as Mg-ion batteries, which consist of Mo_6O_8 (Chevrel phase) cathodes, Mg metal anodes, and Mg organohaloaluminate salt electrolytes (146 Wh kg^{-1})[10,11]. However, Zn/α-MnO_2 Zn-ion batteries show significant capacity fading during long-term cycling and also suffer from poor performance at high current rates. To improve their electrochemical performance, it is essential to elucidate a detailed mechanism of the reaction that occurs at their cathodes. Nevertheless, the exact natures of the redox reactions that occur between α-MnO_2 and zinc ions in Zn-ion batteries are still far from being clearly understood. However, without significant proof or detail, it has been suggested that intercalation of zinc into the tunnels of α-MnO_2 is most likely responsible[7–9]. Here, we report the mechanism of the intercalation of zinc ions into α-MnO_2 (2 × 2 tunnel structure) cathodes during the discharge-charge reactions of

Zn-ion batteries. These reactions involve a reversible phase transition of MnO_2, between tunneled (α-MnO_2) and layered birnessite-like (δ-MnO_2) polymorphs, induced by electrochemical reactions at the cathode.

The crystal structure of α-MnO_2 has one-dimensional 2 × 2 tunnels made of corner- and edge-sharing MnO_6 octahedra along the *z*-axis. The whole structure is stabilized by a small number of cations, such as K^+ (cryptomelane) or Ba^{2+} (hollandite), located at the center of the tunnels[14]. The incorporation of other alkali, alkali-earth, and some post-transition metals into the tunnels or layers of various MnO_2 polymorphs has been the subject of intense research for the past several decades[14–16]. Studies on the electrochemical insertion/de-insertion of Li^+, Na^+, and Mg^{2+} ions into these structures have examined their possible use as cathode materials for Li-ion, Na-ion, and Mg-ion batteries. For instance, a study of Li intercalation into the tunnels of α-MnO_2 showed that more than 0.6 Li atoms per manganese atom go into the channels without significant crystallographic change[17]. In addition, as many as 0.5 Na^+ ions per manganese atom have been shown to incorporate into the S-shaped tunnels of $Na_{0.44}MnO_2$ with a promising cycle performance[18]. However, the insertion mechanism of Zn^{2+} ions is expected to be different than that of Li^+ or Na^+ ions because of the much stronger electrostatic interaction between divalent zinc ions and wall structures, as well as the aqueous electrolyte. We examined the characteristics of discharged and charged cathodes containing a tailor-designed α-MnO_2 nano-rod, using various ex-situ analysis techniques. We have, for the first time, shown that the intercalation of zinc ions into these MnO_2 structures leads to a reversible phase transition, from a tunneled to a layered structure, which involves the dissolution of manganese from the tunnel walls into the electrolyte. We believe that this is a significant finding that can pave the way for drastic improvements in the electrochemical performances of Zn-ion batteries and the accelerated commercialization of this battery system.

Results

Structural and morphological changes of α-MnO_2 during discharge and charge processes. The α-MnO_2 nano-rods were synthesized from $KMnO_4$ by the known hydrothermal method[19]. It is well known that MnO_2 with one-dimensional internal tunnels often crystallizes with a wire or rod-like morphology with tunnels running along the wire or rod axis. In this work, α-MnO_2 nano-rods were used so that any morphological changes could be easily detected following electrochemical reactions. Coin cells containing α-MnO_2 cathodes, zinc metal anodes, and aqueous 1.0 M $ZnSO_4$ electrolyte were employed for electrochemical evaluations. Figure 1a exhibits the discharge-charge profile of a zinc/α-MnO_2 battery for its first two successive cycles using a slow current rate of C/20 and a cycling capacity retention up to 30 cycles (Figure 1a inset). During the first discharge, a potential plateau near 1.3 V can be clearly seen, suggesting that two phases are involved in the electrochemical reaction[20,21]. The observed capacity of α-MnO_2 was approximately 194 mAh g^{-1} for the first cycle and increased to 205 mAh g^{-1} for the second. These values are close to those reported in previous papers[7–9]. Changes to the crystal structure of the α-MnO_2 nano-rods following interaction with zinc ions were investigated by analyzing ex-situ X-ray diffraction (XRD) patterns of the original (**A**), half-discharged (**B**), fully-discharged (**C**), charged (**D**), and 2nd discharged (**E**) cathodes, as shown in Figure 1b. After a full discharge to 0.7 V (**C**), a strong single reflection from a new phase with a *d*-spacing of approximately 7 Å was observed in addition to a few minor reflections, and those of α-MnO_2 disappeared. After charging to 1.9 V (**D**), the new phase disappeared and the original α-MnO_2 structure resurfaced, implying that the process was reversible. At the half-discharge (**B**), a mixture of the α-MnO_2 and the new phase were observed, in accordance with electrochemical

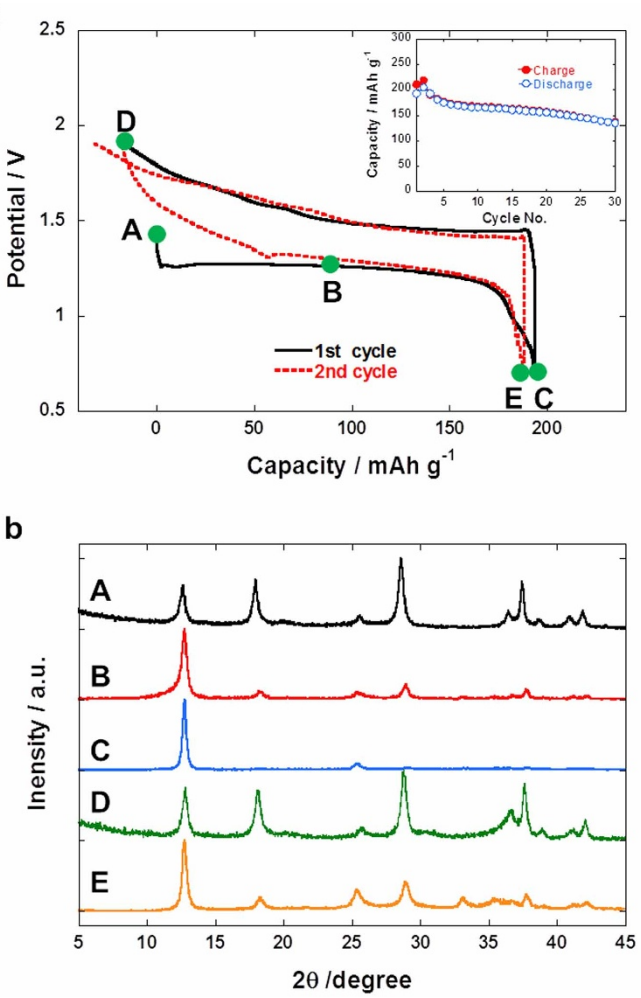

Figure 1 | Investigation of structural changes of the cathode during electrochemical cycling. (a) Potential profiles of the zinc/α-MnO_2 Zn-ion battery during the first (black line) and the second (red line) cycles, and their cycling performance up to 30 cycles (inset). (b) Ex-situ X-ray diffraction patterns of the electrodes at various charge and discharge stages: original electrode (A), half discharged electrode (B), fully discharged electrode (C), fully recharged electrode (D), and fully re-discharged electrode (E), as indicated in Figure 1a.

measurements. After the second discharge (**E**), the new phase reappeared as the main discharge product. Morphological observations of the cathodes, shown in Figure S1 and S2, indicate that the original nano-rod shape and crystallographic integrity of α-MnO_2 are well-preserved throughout the first discharge-charge cycle. Specifically, tunnels or layers, homogenously spaced approximately 7 Å apart, are clearly visible throughout the entire electrochemical process. These observations indicate that the structure of the new phase in the discharged electrode is closely related to that of the original α-MnO_2 and that intercalation is most likely responsible for the electrochemical reaction, as reported previously[7].

Identification of the discharge product. Since the XRD pattern of the discharged electrode in Figure 1 is not informative in clarifying the discharge product due to the lack of useful reflections, transmission electron microscopy (TEM) analysis, using selected area electron diffraction, was carried out on individual nano-rods. Figure 2a shows an electron diffraction pattern of an original α-MnO_2 nano-rod prior to electrochemical cycling. The diffraction pattern was indexed to the [-110] zone of a tetragonal lattice in the I4/m space group. The lattice spacing estimated from the electron

diffraction pattern matched the literature value and XRD data well. A bright field TEM image of the discharged nano-rod is shown in Figure 2b. As can be seen, the nano-rod morphology remained intact after full discharge. However, the non-uniform contrast suggests that the observed nano-rod was likely highly strained. The corresponding electron diffraction pattern, shown in Figure 2c, was indexed to the [012] zone of triclinic chalcophanite ($ZnMn_3O_7 \cdot 3H_2O$) (space group P-1, lattice parameters from the literature are $a = 7.54$ Å, $b = 7.54$ Å, $c = 8.22$ Å, $\alpha = 90^\circ$, $\beta = 117.2^\circ$, $\gamma = 120^\circ$)[22,23]. In order to ascertain the correct indexing of the diffraction pattern, a simulated kinematic electron diffraction pattern of the [012] zone, produced using WebEMAPS[24] and the structural parameters provided from the literatures[22,23], is shown in Figure 2d. Two diffraction vectors, (100) and (-121), are denoted in Figures 2c and 2d to illustrate that the two patterns (experimental and simulated) match each other. The similar analysis for other zones such as [2–10] zone (Figure 2e,f), [310] zone (Figure S3b), [1–40] zone (Figure S3c) for the discharged nano-rod accordantly indicates that the structure of discharge product is that of triclinic chalcophanite. The electron diffraction and chemical analysis of the discharged product (Figure S4) suggest that the α-MnO_2 nanorods underwent a structural phase transition during discharge to form Zn-birnessite, a triclinic chalcophanite-like layered structure. To further support this, Zn-birnessite was synthesized by ion exchange of Na-birnessite at 160°C, in an aqueous $ZnSO_4$ solution, (see Methods). Its XRD pattern was then compared to that of the discharge product, Figure 3a. The XRD pattern of the discharge product corresponded well to that of the Zn-birnessite. From these observations, it is concluded that the structure of the discharge product is most likely an analogue of mineral chalcophanite ($(Zn, Mn)Mn_3O_7 \cdot 3H_2O$) with P-1 space group[22,23]. The structure of chalcophanite closely resembles that of layered Na-birnessite ($Na_4Mn_{14}O_{27} \cdot 9H_2O$), in which intercalated Zn^{2+} ions sit above and below Mn vacancy sites within the layers and form octahedra by coordinating with three oxygen atoms from water molecules and three oxygen atoms from the Mn vacancy sites, below[22,23,25,26]. In contrast to Na-birnessite, the chalcophanite structure is stable even in the absence of water and has been widely investigated to clarify the structure of the birnessite family. When the number of Zn ions intercalated into layers is not large, Zn ions accommodate tetrahedral coordination with three oxygen atoms, from Mn vacancy sites, and one from a water molecule[25,26]. In chalcophanite, it is known that one in seven Mn sites in a layer is vacant. The space group of chalcophanite was initially thought to be P-1[22,23] but later, more detailed investigations have reassigned it to R-3[27]. Both structures consist of stacked MnO_6 layers with interplanar distances of approximately 7 Å. However, the positions of the Zn ions, water molecules, and Mn vacancies within the layers are slightly different. In the present case, the electrochemically induced phase transition of α-MnO_2 to Zn-birnessite, and the persistence of K^+ ions from the α-MnO_2 phase within the Zn-birnessite layers may slightly distort the structure, making it triclinic. The triclinic version of chalcophanite may also be similar to Jianshuiite ($(Mg, Mn)Mn_3O_7 \cdot 3H_2O$), which is a Mg-intercalated birnessite having in the P-1 space group[28]. To further confirm the discharge product, we investigated the oxidation state of the manganese in the electrode by measuring Mn K-edge X-ray absorption spectra, shown in Figure 3b. At the Mn K-edge, the selection rule for electrical dipolar transitions ($\Delta l = \pm 1$) requires that a 1s electron jump to an empty 4p orbital ($1s^2 4p^0 \rightarrow 1s^1 4p^1$). The position of the absorption edge is affected by the oxidation state of the central absorbing atom[29,30]. From Figure 3b, the oxidation state of the manganese in the discharged material is estimated to be nearly identical to that of the Zn-birnessite synthesized from Na-birnessite using the hydrothermal method. Therefore, Zn-birnessite is certainly the main discharge product remaining at the electrode.

Intercalation mechanism of zinc ions into α-MnO_2. From the above observations, the principal discharge product on the electrode is, unequivocally, triclinic Zn-birnessite. But, Mn K-edge absorption spectra, shown in Figure 3b, indicate that the average oxidation state of manganese for the discharged electrode increases, then remains almost unchanged upon further recharging, since the Mn K-edge moves to higher energies as oxidation state increases[29,30]. However, it is not logical for the discharge product to have a higher manganese oxidation state than the original electrode. Therefore, it is reasonable to postulate that some manganese goes into the electrolyte in the form of Mn^{2+} ions, leaving Mn vacancy sites in the electrode. This can occur as the manganese in α-MnO_2 is reduced from tetravalent to trivalent, upon electrochemical intercalation of zinc ions, and Mn^{3+} disproportionates into Mn^{4+} and Mn^{2+} according to the following reactions.

$$Mn^{4+}(s) + e^- \rightarrow Mn^{3+}(s) \quad (1)$$

$$2Mn^{3+}(s) \rightarrow Mn^{4+}(s) + Mn^{2+}(aq) \quad (2)$$

The dissolved Mn^{2+} ions accumulate in the electrolyte during discharge. Considering the fact that the solubility of Mn^{2+} ions in water is typically high (for $MnSO_4$, 70 g per 100 mL of water at 7°C), this implies that the mass of the cathode decreases as discharge proceeds and that a substantial number of manganese ions have been dissolved into the electrolyte by the end of the discharge process. It is well known that Mn^{3+} ions, having a high-spin d^4 ($=t_{2g}^3 e_g^1$) electronic configuration in octahedral symmetry, are highly unstable, due to the Jahn-Teller effect, and susceptible to structural transformations[30–32]. This structural instability often triggers a disproportionation reaction, resulting in the dissolution of some manganese and the destruction of the original structure of the host material. To confirm this, the amounts of Mn in the electrolyte at various stages of the charge/discharge cycle were evaluated by analyzing Mn/Zn ion ratios of the electrolyte, using atomic absorption spectroscopy (AAS). As shown in Figure 3c, the amount of Mn increased as the discharge process proceeded, reaching a maximum at the end of the discharge process. Compared to the concentration of zinc ions in the electrolyte (1.0 mol/L), the amount of Mn, following discharge, corresponds to approximately 1/3 of the total manganese in the electrode (see Methods for the calculation). During charging, the Mn concentration of the electrolyte became negligibly small, which means that dissolved Mn^{2+} ions returned to combine with Mn vacancy sites of the layered structure and were oxidized to become Mn^{3+} and Mn^{4+}.

$$Mn^{2+}(aq) \rightarrow Mn^{4+}(s) + 2e^- \quad (3)$$

Therefore, the manganese in the electrode maintains a high oxidation state throughout the entire discharge-charge process, as observed in the Mn K-edge spectra presented in Figure 3b. It is surprising that almost 1/3 of the manganese of the original α-MnO_2 structure is dissolved during discharge to become Zn-birnessite, nevertheless it is fully recovered to form the original α-MnO_2 structure upon recharging. The α-MnO_2 has one-dimensional 2×2 and 1×1 tunnels, comprised of four identical cross-linking double chains of MnO_6 octahedra, that extend along the ***c***-axis, the edges of which are connected by corner-sharing MnO_6 octahedra, as described in Figure 4. Conversely, Zn-birnessite has a layered structure with an interlayer spacing of approximately 7 Å, which is similar to the size of the tunnels of α-MnO_2 (Zn-birnessite with P-1 space group is shown in Figure 4). In fact, the crystal structure of Zn-birnessite would be closely related to that of α-MnO_2 if there were bridges connecting adjacent layers in Zn-birnessite. Therefore, noting the similarities of the crystal structures of α-MnO_2 and Zn-birnessite, it is reasonable to assume that during discharge the

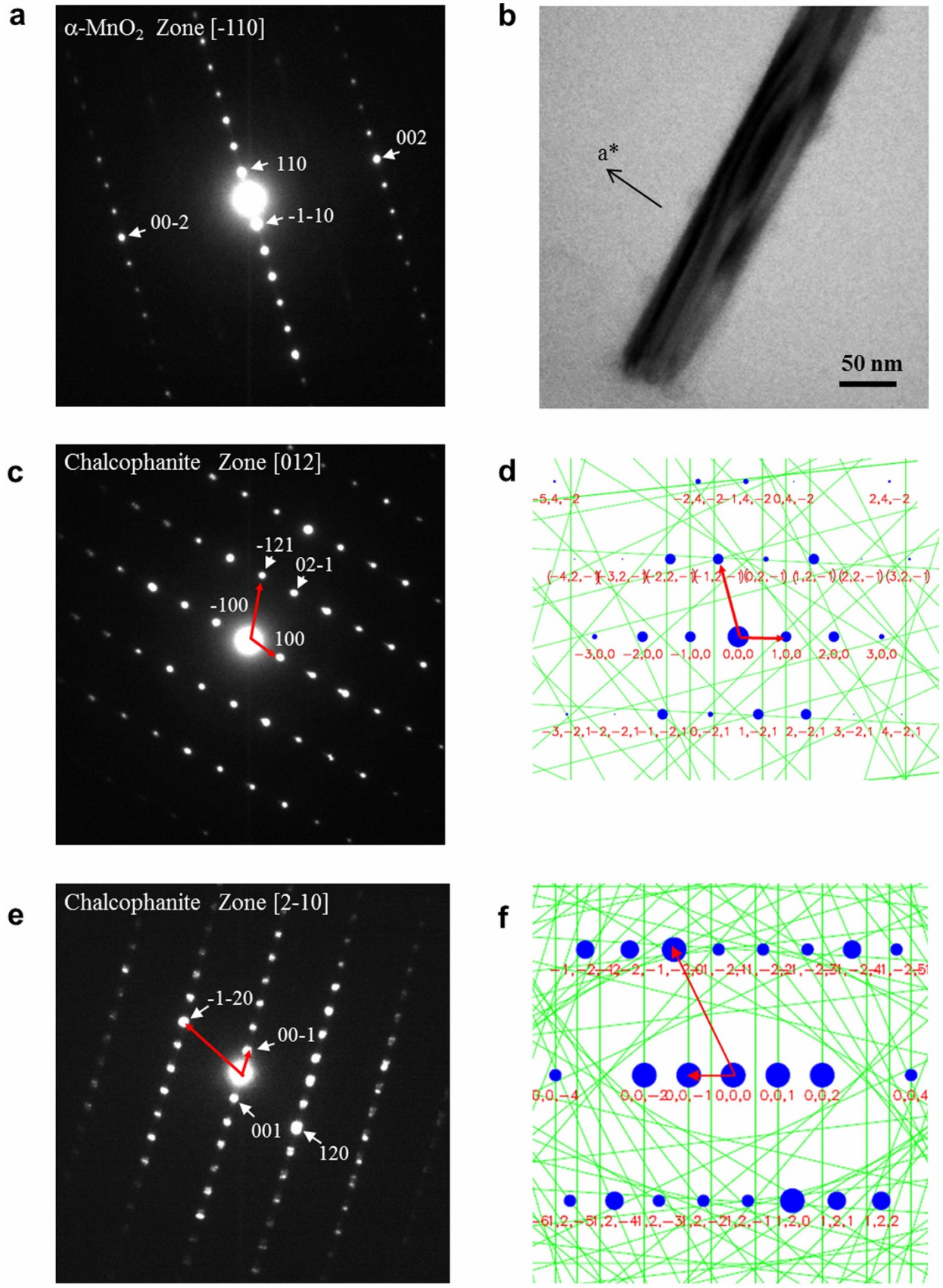

Figure 2 | Identification of the discharge product by analysis of selected area electron diffraction patterns. (a) Electron diffraction pattern of the original α-MnO_2 nanorod, indexed to the [-110] zone of a tetragonal lattice with space group I4/m, (b) a bright field TEM image of the discharged nanorod, (c) its corresponding electron diffraction pattern, indexed to the [012] zone of a triclinic lattice with space group P-1, and (d) a simulated kinematic electron diffraction pattern of the [012] zone produced using WebEMAPS[24] and the structural parameters provided in the main text, while (e) and (f) represent those patterns indexed to the [2–10] zone.

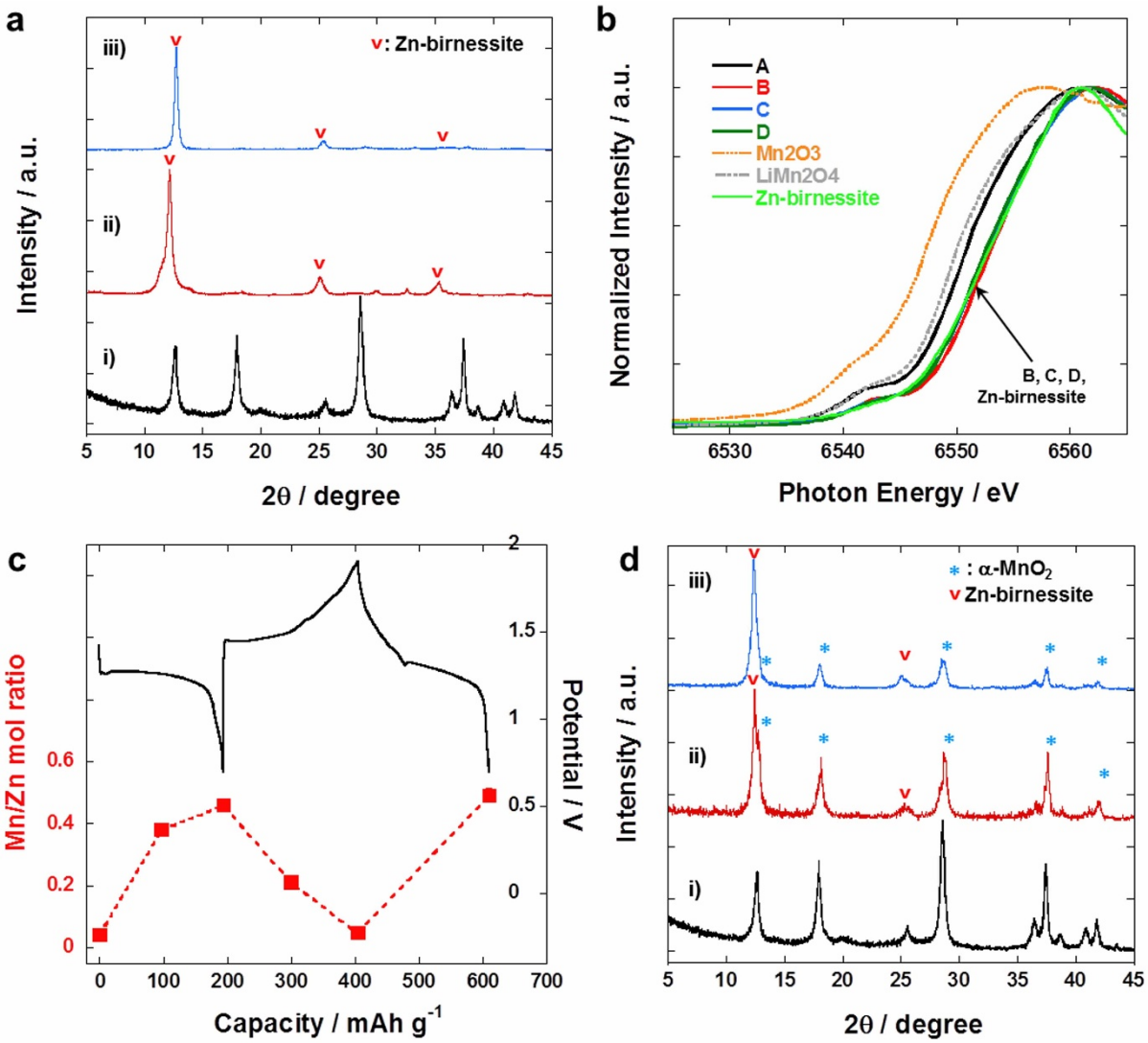

Figure 3 | Characterization of the discharge product. (a) Comparison of X-ray diffraction patterns of i) as-prepared α-MnO_2, ii) hydrothermally prepared Zn-birnessite, and iii) a fully discharged electrode. (b) Mn K-edge X-ray absorption spectra for as-prepared α-MnO_2 and electrodes at various discharge and charge stages, as indicated in Figure 1a. (b) also include reference spectra for Mn_2O_3, $LiMn_2O_4$, and Zn-birnessite. (c) Mn/Zn mol ratio in the electrolyte (red square), measured by AAS during electrochemical cycling, and the discharge-charge profile (black). (d) X-ray diffraction patterns of i) as-prepared α-MnO_2, and the product prepared by hydrothermally-treating α-MnO_2 for ii) 24 h and iii) 72 h.

MnO_6 units of two opposite chains of α-MnO_2 undergo destructive dissolution and that Mn vacancies form in the upper and underlying layers. Furthermore, during recharging, Mn^{2+} ions intercalate back into the layers and start to form bridges between layers. Transformations of a phyllomanganate such as layered birnessite to other structurally-related polymorphs of MnO_2, like buserite and todorokite, have been well documented and typically involve hydrothermal processes at elevated temperatures[33,34]. It has been reported that chalcophanite also can be prepared from Na-birnessite by ion exchange[15]. However, an electrochemically triggered reversible transformation between these polymorphs has not yet been reported, to the best of our knowledge. To investigate if Zn-birnessite can be prepared by chemical means from α-MnO_2, 1.0 M $ZnSO_4$ solutions (the same composition as the electrolyte) containing α-MnO_2 were hydrothermally treated at 160°C for various durations. The results presented in Figure 3d show that the Zn-birnessite phase grows slowly from α-MnO_2 as the reaction proceeds. Therefore, the structure of Zn-birnessite is closely related to that of α-MnO_2 and the formation of Zn-birnessite by zinc ion intercalation into α-MnO_2, and the accompanying Mn dissolution and vacancy formation, is a thermodynamically favorable process.

Discussion

Since a lot of manganese from the cathode is dissolved into the electrolyte during discharge, it was important to determine if the dissolved Mn^{2+} ions caused parasitic reactions and to confirm that they returned to the cathode to take part in the charging reaction. For instance, Mn^{2+} ions may be deposited on the anode instead of returning to the cathode during charging, which could give rise to significant capacity fading. However, compositional analysis on the anodes after the 1st and the 10th charge showed no manganese was deposited on the surface (Figure S5). Since the standard electrode potential for the electro-reduction of manganese, $Mn^{2+} + 2e^- \rightarrow Mn^0$, $E^0 = -1.185$ V (vs. NHE), is much lower than that for zinc, $Zn^{2+} + 2e^- \rightarrow Zn^0$, $E^0 = -0.763$ V (vs. NHE) or hydrogen evolution, $2H^+ + 2e^- \rightarrow H_2$, $E^0 = -0.237$ V (vs. NHE, at pH = 4), it is unlikely that any meaningful amount of manganese is deposited on the zinc anode. The anodic potential sweep curves for the α-MnO_2 electrode with and without a prior discharge in Figure 5a shows bulky electrolyte decomposition occurs only at those potentials above 2.0 V vs. Zn/Zn^{2+}. Therefore, charging reaction can be best explained by the layered to tunneled transition of MnO_2. To further confirm that manganese ions dissolved in the electrolyte participate in the elec-

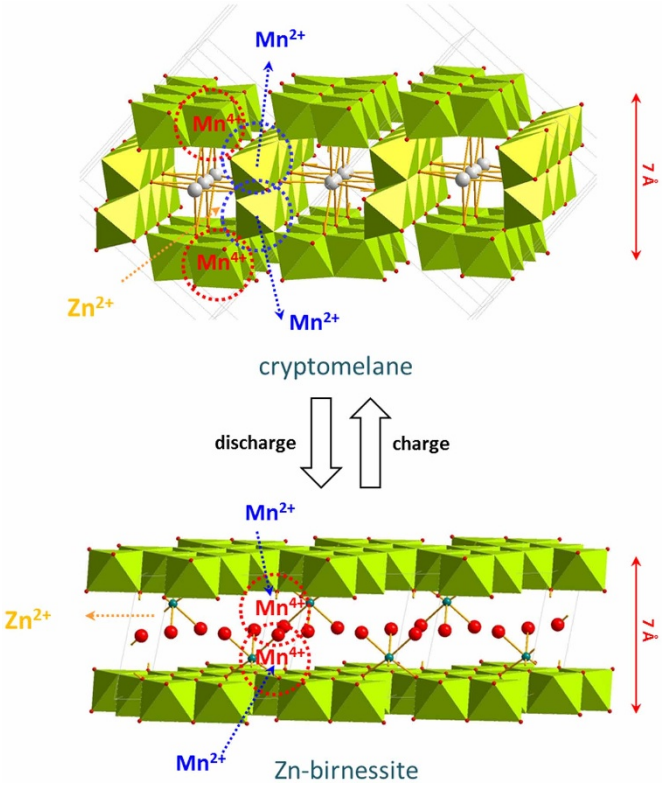

Figure 4 | Schematic illustrating the mechanism of zinc intercalation into α-MnO_2. α-MnO_2 with a 2 × 2 tunnel structure incorporates zinc ions during discharge. This leads to dissolution of manganese from the wall and the formation of vacancies in the upper/underlying layers. A slight distortion of the overall structure results in Zn-birnessite with a triclinic lattice. During charging, Mn^{2+} ions are reversibly inserted back into the layers to reform the tunneled structure. Green octahedra and white, red, and turquoise spheres represent MnO_6, K^+, H_2O, and Zn^{2+}, respectively.

trochemical reaction during the charge process, a cell containing α-MnO_2 cathode was first discharged and then dismantled to recover the discharged cathode. The cathode was washed with deionized water and was placed in the fresh coin cell with a fresh electrolyte. Then, the cell was subject to charging process. As it was clear in Figure 5b, the cell could hardly be charged, implying that manganese ions, indeed, diffused back to the cathode to join in the electrochemical reaction for the formation of α-MnO_2 during charge process. Figure S6 shows charge-discharge profiles at the 1st, the 5th, and the 10th cycles and XRD patterns of fully-discharged and fully-charged electrodes at those cycles. They shows that while Zn-birnessite and α-MnO_2 still forms at later cycles after discharge and charge process, respectively, amorphous phase grows as cycle proceeds. An excessive structural stress developed by the repeated phase transitions probably caused the gradual destruction of the original structure and the conversion to amorphous phase. The discharge-charge profiles at the various current densities were shown in Figure S7. It shows a discharge capacity of 120 mAh g^{-1} at 1 C rate, which is about 60% of that at C/10. Interestingly, the increase in the overpotential at the high current rates for the discharge process was much larger than that for the charge. This is probably due to the fact that zinc ions intercalates into one-dimensional narrow 2 × 2 tunnels and Jahn-Teller cation, Mn^{3+}, is formed during discharge process, whereas two dimensional channels in the layered Zn-birnessite facilitate the fast diffusion of zinc and manganese ions during charge process.

In conclusion, we have reported the intercalation mechanism of zinc ions into α-MnO_2 during the discharging and charging in Zn-ion batteries. The mechanism involves a reversible phase transition between tunneled (α-MnO_2) and layered (Zn-birnessite) MnO_2 polymorphs which is induced by electrochemical reactions at the cathode. The formation of unstable Mn^{3+} on the wall of α-MnO_2 triggers the dissolution of manganese into the electrolyte during discharge. However, manganese ions are reversibly inserted into the layers of Zn-birnessite during charging. Research into other types of tunneled MnO_2, such as todorokite and $Na_{0.44}MnO_2$, is currently being conducted, the results of which will be reported in our later communications.

Methods

Preparation of α-MnO_2 nano-rod. Crystalline α-MnO_2 nano-rods were synthesized by a previously reported hydrothermal method[19]. Briefly, $KMnO_4$ (0.1264 g) and NH_4Cl (0.0428 g) were mixed together with distilled water (40 mL) until completely dissolved. The solution was then poured into a Teflon-lined container and subjected to heat-treatment at 140°C for 24 h. Next, the product was filtered and washed with plenty of distilled water. Finally, the filtered powder was dried in a vacuum oven at 80°C for 24 h.

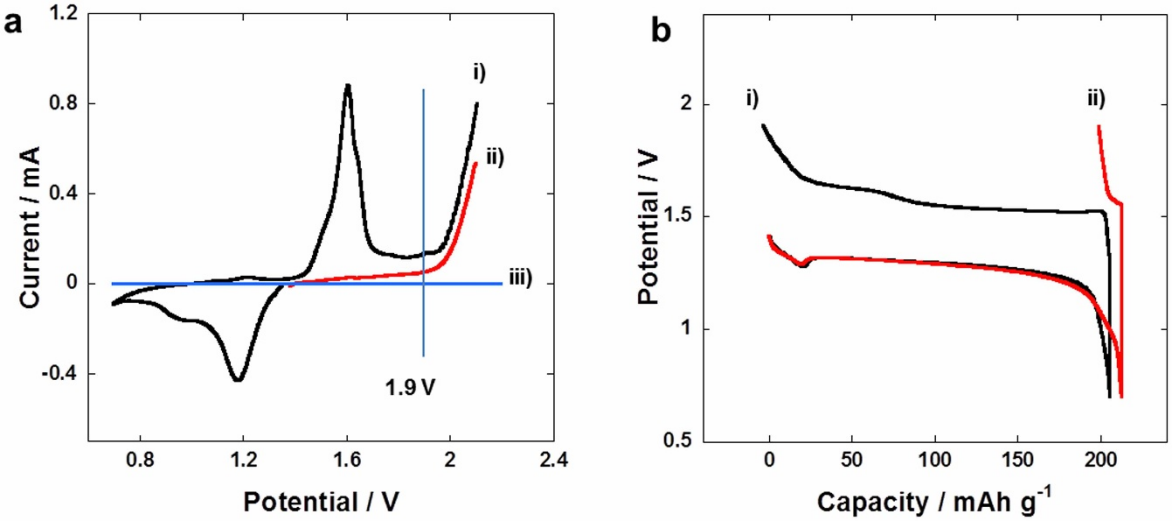

Figure 5 | Characterization of the electrochemical cell containing α-MnO_2 electrode. (a) The electrode with α-MnO_2 was potentiodynamically charged at a scan rate of 0.02 mV sec^{-1} (i) with and (ii) without prior discharge until major electrolyte decomposition occurs. The curve (iii) represents the background current where an electrode without α-MnO_2 is used. (b) The discharge-charge curves at the 1st cycle for (i) the normal cell and (ii) the one which cell components and electrolyte were replaced by fresh ones after the 1st discharge.

Preparation of Zn-birnessite from Na-birnessite. For the synthesis of Na-birnessite, a 1.0 M $MnSO_4 \cdot H_2O$ solution (20 mL) was mixed with a 6.0 M NaOH solution (30 mL), to which a mixture of $(NH_4)_2S_2O_8$ (3.2 g) and $MgSO_4 \cdot 7H_2O$ (0.7 g) were slowly added and stirred for 2 h. After filtering, Na-birnessite was dispersed in a 1.0 M $ZnSO_4$ solution (300 mL) and stirred for 24 h. Finally, Zn-birnessite was obtained by pouring the slurry into a hydrothermal reactor and heat-treating it at 160°C for 24 h. After it cooled down, the product was washed thoroughly with plenty of distilled water and dried in a vacuum oven overnight at 80°C.

Preparation of Zn-birnessite from α-MnO_2. The α-MnO_2 nano-rods were dispersed in a 1.0 M $ZnSO_4$ solution (300 mL) and stirred for 24 h. Then the whole slurry was poured into a hydrothermal reactor and heat-treated at 160°C for the desired duration (24 h and 72 h). After cooling, the product was washed thoroughly with plenty of distilled water and dried in a vacuum oven overnight at 80°C.

Electrochemical measurements. For the preparation of the cathode, synthetic α-MnO_2 powder (70 mg) and carbon black (10 mg) were mixed together with a spatula. Polyvinylidene fluoride (PVdF) binder (20 mg) was then added and the whole mixture was ball-milled in N-methyl-2-pyrrolidone (NMP). The α-MnO_2 slurry was cast onto stainless steel foil (25 μm thickness) at a loading of approximately 5.0 mg cm^{-2}. 2032 type coin cells were used to evaluate the electrochemical properties of the electrode and were composed of the as-prepared cathode, a zinc foil anode (10 μm thickness), a glass wool separator, and a 1.0 M aqueous zinc sulfate ($ZnSO_4$) electrolyte. The cell test was carried out with a MACCOR cycler between 0.7–2.0 V at a C/20 rate for the initial 2 cycles, then at a C/5 rate for the remaining cycles (1 C = 210 mA g^{-1} of α-MnO_2). The performance at various current rates was investigated similarly by cycling at C/20 for the initial 2 cycles, then at the desired current rates (C/10, C/5, C/2, C/1) for 5 cycles.

Characterization. The crystallographic structures were measured by powder X-ray diffraction (XRD) using Cu-$K_{\alpha 1}$ radiation (λ = 1.5405 Å, Rigaku D/MAX-2500/PC). The morphology of the α-MnO_2 electrodes was observed by high resolution transmission electron microscopy (HR-TEM, FEI Tecnai G2 operating at 200 KeV) and field-emission scanning electron microscopy (FE-SEM, Hitachi S-4000). Mn K-edge X-ray absorption spectra were measured in transmission mode at the 10D beamline of the Pohang Accelerator Laboratory. Absorption was recorded from 6535–6565 eV at intervals of 0.5 eV. The amount of Zn and Mn dissolved in the $ZnSO_4$ electrolyte was measured by atomic absorption spectroscopy (AAS, Thermo Electron Corporation, SOLAAR M). The cathode containing α-MnO_2 was cycled to the desired state of discharge or charge as indicated in Figure 3c. Then, the cell was taken apart from which a separator containing the electrolyte was recovered. Then, the separator was put into the glass bottle containing deionized water (5.0 mL) and stored for 1 day before AAS analysis.

Calculation of the amount of Mn dissolved during discharge and charge. The amount of electrolyte used for each cell was approximately 85 μL. The molar concentration ratio of Mn/Zn in the electrolyte of the discharged cell, as determined by AAS, was ~0.46. This means that the actual Mn concentration of the electrolyte was approximately 0.46 mol/L. Thus, the amount of Mn in 85 uL of electrolyte was approximately 0.039 mmol. A typical mass of α-MnO_2 on cathode is ~10 mg. Thus, the amount of Mn on cathode was approximately 0.115 mmol. Therefore, the fraction of Mn dissolved in the electrolyte out of the original Mn in α-MnO_2 is approximately 34%.

1. Post, J. E. Manganese oxide minerals: Crystal structures and economic and environmental significance. *Proc. Natl. Acad. Sci.* **96**, 3447–3454 (1999).
2. Thackeray, M. M. Manganese oxides for lithium batteries. *Prog. Solid St. Chem.* **25**, 1–71 (1997).
3. Neburchilov, V., Wang, H., Martin, J. J. & Qu, W. A review on air cathodes for zinc-air fuel cells. *J. Power Sources* **195**, 1271–1291 (2010).
4. Gritter, R. J. & Wallace, T. J. The manganese dioxide oxidation of allylic alcohols. *J. Org. Chem.* **24**, 1051–1056 (1959).
5. Villalobos, M., Lanson, B., Manceau, A., Toner, B. & Sposito, G. Structural model for the biogenic Mn oxide produced by Pseudomonas putida. *Am. Mineral.* **91**, 489–502 (2006).
6. Chabre, Y. & Pannetier, J. Structural and electrochemical properties of the proton/γ-MnO_2 system. *Prog. Solid St. Chem.* **23**, 1–130 (1995).
7. Xu, C., Li, B., Du, H. & Kang, F. Energetic zinc ion chemistry: The rechargeable zinc ion battery. *Angew. Chem. Int. Ed.* **51**, 933–935 (2012).
8. Xu, C., Li, B., Chiang, S. W., Ma, J. & Kang, F. Investigation on zinc ion storage in alpha manganese dioxide for zinc ion battery by electrochemical impedance spectrum. *J. Electrochem. Soc.* **160**, A93–A97 (2013).
9. Lee, J., Ju, J. B., Cho, W. I., Cho, B. W. & Oh, S. H. Todorokite-type MnO_2 as a zinc-ion intercalating material. *Electrochimica Acta* **112**, 138–143 (2013).
10. Aurbach, D. *et al.* Prototype systems for rechargeable magnesium batteries. *Nature* **407**, 724–727 (2000).
11. Levi, E., Gofer, Y. & Aurbach, D. On the way to rechargeable Mg batteries: The challenge of new cathode materials. *Chem. Mater.* **22**, 860–868 (2010).
12. Jayaprakash, N., Das, S. K. & Archer, L. A. The rechargeable aluminum-ion battery. *Chem. Commun.* **47**, 12610–12612 (2011).
13. Wang, W. *et al.* A new cathode material for super-valent battery based on aluminum ion intercalation and deintercalation. *Sci. Rep.* **3**, 3383; DOI:10.1038/srep03383 (2013).
14. Feng, Q., Yanagisawa, K. & Yamasaki, N. Hydrothermal soft chemical process for synthesis of manganese oxides with tunnel structures. *J. Porous Mater.* **5**, 153–161 (1998).
15. Aronson, B. J., Kinser, A. K., Passerini, S., Smyrl, W. H. & Stein, A. Synthesis, characterization, and electrochemical properties of magnesium birnessite and zinc chalcophanite prepared by a low-temperature route. *Chem. Mater.* **11**, 949–957 (1999).
16. Duncan, M. J., Leroux, F., Corbett, J. M. & Nazar, L. F. Todorokite as a Li insertion cathode. *J. Electrochem. Soc.* **145**, 3746–3757 (1998).
17. Rossouw, M. H., Liles, D. C., Thackeray, M. M., David, W. I. F. & Hull, S. Alpha manganese dioxide for lithium batteries: A structural and electrochemical study. *Mat. Res. Hull.* **27**, 221–230 (1992).
18. Cao, Y. *et al.* Reversible sodium ion insertion in single crystalline manganese oxide nanowires with long cycle life. *Adv. Mater.* **23**, 3155–3160 (2011).
19. Gao, Y., Wang, Z., Wan, J., Zou, G. & Qian, Y. A facile route to synthesize uniform single-crystalline α-MnO_2 nanowires. *J. Cryst. Growth* **279**, 415–419 (2005).
20. Delmer, O., Balaya, P., Kienle, L. & Maier, J. Enhanced potential of amorphous electrode materials: Case study of RuO_2. *Adv. Mater.* **20**, 501–505 (2008).
21. Yamada, A. *et al.* Room-temperature miscibility gap in Li_xFePO_4. *Nat. Mater.* **5**, 357–360 (2006).
22. Wadsley, A. D. Interstitial atoms in the layer structure $ZnMn_3O_7$ $3H_2O$ (chalcophanite). *Nature* **172**, 1103–1104 (1953).
23. Wadsley, A. D. The crystal structure of chalcophanite, $ZnMn_3O_7 \cdot 3H_2O$. *Acta Cryst.* **8**, 165–172 (1955).
24. Zuo, J. M. & Mabon, J. C. Web-based Electron Microscopy Application Software: Web-EMAPS, Microsc Microanal 10 (Suppl 2), URL: http://emaps.mrl.uiuc.edu/, (2004) (date of access: 08/04/2014).
25. Kwon, K. D., Refson, K. & Sposito, G. Zinc surface complexes on birnessite: A density functional theory study. *Geochim. Cosmochim. Acta* **73**, 1273–1284 (2009).
26. Toner, B., Manceau, A., Webb, S. M. & Sposito, G. Zinc sorption to biogenic hexagonal-birnessite particles within a hydrated bacterial biofilm. *Geochim. Cosmochim. Acta* **70**, 27–43 (2006).
27. Post, J. E. & Appleman, D. E. Chalcophanite, $ZnMn_3O_7 \cdot 3H_2O$: New crystal-structure determinations. *Am. Miner.* **73**, 1401–1404 (1988).
28. Jambor, J. L. & Grew, E. S. New mineral names. *Am. Mineral.* **79**, 185–189 (1994).
29. Mehadji, C., Nour, S. & Chermette, H. X-ray absorption of tetraoxomanganates (MnO_4^{n-}): experimental and MS LSD computational studies. *Chem. Phys.* **148**, 95–102 (1990).
30. Kobayahi, S., Kottegoda, I. R. M., Uchimoto, Y. & Wakihara, M. XANES and EXAFS analysis of nano-size manganese dioxide as a cathode material for lithium-ion batteries. *J. Mater. Chem.* **14**, 1843–1848 (2004).
31. Thackeray, M. M. *et al.* Structural fatigue in spinel electrodes in high voltage (4 V) Li/$Li_xMn_2O_4$ cells. *Electrochem. Solid-State Lett.* **1**, 7–9 (1998).
32. Berg, H., Göransson, K., Nölang, B. & Thomas, J. O. Electronic structure and stability of the $Li_xMn_2O_4$ ($0 < x < 2$) system. *J. Mater. Chem.* **9**, 2813–2830 (1999).
33. Golden, D. C., Chen, C. C. & Dixon, J. B. Transformation of birnessite to buserite, todorokte, and manganite under mild hydrothermal treatment. *Clays Clay Miner.* **35**, 271–280 (1987).
34. Feng, Q. Metal ion extraction/insertion reactions with todorokite-type manganese oxide in the aqueous phase. *Chem. Mater.* **7**, 1722–1727 (1995).

Acknowledgments

This work was supported by the Green City Technology Flagship Program funded by the Korea Institute of Science and Technology (KIST-2013-2E23996).

Author contributions

S.H.O. developed the concept and designed the experiments, and B.L. carried out most of the experimental work. C.S.Y. conducted the experiments involving TEM and analyzed SAED patterns. H.R.L., K.Y.C. and B.W.C. helped with the measurement for X-ray absorption spectroscopy.

Additional information

Supplementary information accompanies this paper at http://www.nature.com/scientificreports

Competing financial interests: The authors declare no competing financial interests.

How to cite this article: Lee, B. *et al.* Electrochemically-induced reversible transition from the tunneled to layered polymorphs of manganese dioxide. *Sci. Rep.* **4**, 6066; DOI:10.1038/srep06066 (2014).